Journal of Computational Physics 442 (2021) 110480

Contents lists available at ScienceDirect

Journal of Computational Physics

www.elsevier.com/locate/jcp

Three dimensional modeling of liquid droplet spreading on solid surface: An enriched finite element/level-set approach

Mohammad R. Hashemi [a,b,*], Pavel B. Ryzhakov [a,b], Riccardo Rossi [a,b]

[a] Centre Internacional de Mètodes Numèrics en Enginyeria (CIMNE), 08034 Barcelona, Spain
[b] Universitat Politècnica de Catalunya (UPC), 08034 Barcelona, Spain

ARTICLE INFO

Article history:
Available online 2 June 2021

Keywords:
Two-phase flow
Surface tension
Wetting
Microfluidics
Droplets
Contact-line

ABSTRACT

A physically consistent approach is introduced to simulate dynamics of droplets in contact with solid substrates. The numerical method is developed by introducing the molecular–kinetic model within the framework of the level-set/enriched finite element method and including the theoretically resolved sub-elemental hydrodynamics. The level-set method is customized to comply fully with the model acquired for the moving contact-line. The consistency of the proposed method is verified by comparing the simulation results with the theoretical predictions. In order to further validate the method, the spreading of a droplet is numerically modeled and compared rigorously with the experimental data reported in the literature. The proposed method is also employed to capture the evolution of a droplet trapped in a conical pore. All test-cases are simulated on three-dimensional computational domains.

1. Introduction

Accurate modeling of liquid spreading on a solid surface [1] is of a fundamental importance in the analysis of multi-phase flows in micro-channels [2,3] as well as porous [4] and fibrous [5] media, which are encountered in a wide range of industrial applications. One such application, that motivated the developments of the present work, is the water-air transport in the gas channels and fibrous diffusion layer of polymer electrolyte membrane fuel cells (PEMFCs) [6,7] that is an essential factor in the determination of the performance of the cell [8,9].

In the modeling of phenomena associated with the multi-phase flow in the presence of a solid substrate, one of the major challenges is to deal with the moving boundary of the three-phase (gas/liquid/solid) interface, the so-called contact-line, using an appropriate condition [10,11]. Theoretical investigations of the movement of the contact-line [12,13] imply that the classical continuum-level hydrodynamics along with the conventional no-slip condition at the solid surface lead to an unbounded velocity gradient and consequently a singularity in the stress at the contact-line. The conventional approach to alleviate this singularity is to take into account a slip condition in the vicinity of the contact-line [14,15], for which there is also some evidence from molecular dynamics simulations [16–18].

Employing the slip condition in the context of the continuum hydrodynamics allows for a theoretical solution for the viscous bending phenomenon and leads to the well-established Cox's relation [19], which gives a correlation between the apparent macroscopic contact-angle and the microscopic contact-angle. More recently, it was shown that alleviating the

* Corresponding author at: Universitat Politècnica de Catalunya (UPC), 08034 Barcelona, Spain.
E-mail addresses: mhashemi@cimne.upc.edu (M.R. Hashemi), pavel.ryzhakov@upc.edu (P.B. Ryzhakov), rrossi@cimne.upc.edu (R. Rossi).

https://doi.org/10.1016/j.jcp.2021.110480

stress singularity can result in a complement to the hydrodynamic theory; Zhang and Mohseni [20] explored the possibility of integrating the singular stress in the close vicinity of the contact-line in order to obtain a model for the dynamic microscopic contact-angle.

Besides the hydrodynamic theory that focuses on the phenomena at the continuum level, molecular–kinetic theory [21] has also been acquired to derive a model for the moving contact-line. It was shown that the resulting model is consistent with the results of the molecular dynamics simulations [22,23]. Both the Cox's relation and the molecular–kinetic model have been examined by fitting the experimentally observed correlation between the contact-angle and the contact-line velocity [24–26].

It had been revealed that depending on the features of the set of experiments, one model or another provides a better match [27–29]. This can be explained as a result of the fact that the hydrodynamic theory accounts for the viscous dissipation while the molecular–kinetic theory focuses on the energy dissipation in a very close vicinity of the contact-line [26]. Thus, depending on the flow configuration and the velocity of the contact-line, either of these mechanisms is dominant and the behavior can be better characterized with the respective model. Based on the experimental results, due to the ambiguity in determining the underlying physics and the lack of a systematic approach to determine constitutive parameters [30,20], it is not a straightforward task to decide which theory (and the resulting) model should be employed. Therefore, in order to exploit the pros of both the theories, combined models were proposed [31–35], in which the frictional contact-line slip is taken into account as well as the viscous dissipation. Recently, utilizing a series of molecular dynamics simulations, Fernández-Toledano et al. [36] stated that the hydrodynamic theory is a reliable means for correlating the apparent (experimentally measurable) contact–angle and the microscopic contact–angle, while the molecular–kinetic theory governs the dynamic microscopic contact–angle. This confirms the rationale of developing combined models like the one proposed by Petrov and Petrov [31].

In the context of the numerical modeling of the dynamics of the contact-line, the utilization of the generalized Navier-slip condition [37–39] is a viable choice [40]. Being based on the combination of the Navier-slip condition on the solid substrate and the frictional movement of the contact-line due to the unbalanced Young stress, it is consistent with the molecular dynamics simulations [37,39] and the thermodynamic principles [30,41] for modeling the wetting phenomena. The generalized Navier-slip condition has so far been applied in the numerical simulation of various cases involving moving contact-line [42–45]. A numerically different, but fundamentally similar approach is the direct imposition of a friction force at the contact-line along with the standard Navier-slip condition [46]. In the numerical modeling, it is also possible to impose the no-slip condition on the solid surface while the force singularity is circumvented by modifying the conventional formulation [39]; as a notable choice, diffusion can be introduced as the mechanism underlying the contact-line movement [47] similar to the diffuse interface methods [48–50]. Nevertheless, this approach is out of the scope of the present paper and will not be further discussed here.

Besides the utilized slip condition, one of the fundamental issues with the computational methods applied to the moving contact-line problem is the mesh-dependence of the results [51,52]. A physical and a numerical factor, at least partially, responsible for this issue are the unresolved sub-grid hydrodynamics and the interfacial force smoothing, respectively. In the vicinity of the contact-line, hydrodynamic mechanisms act at a small length-scale which, even being far beyond the molecular–scale, cannot be adequately resolved unless a prohibitive refinement of the computational mesh is performed [53]. The hydrodynamic theory is a means to circumvent the need for such refinement [54] and helps improving the mesh-independence of the numerical results [55–57]. On the other hand, conventional numerical methods typically utilize a numerically smooth representation of the physically localized surface tension [58–60] following the so-called "continuum force approach" [61]. In the presence of the moving contact-line, the unbalanced Young stress is also smoothed out to act similar to a body force centralized at the contact-line [62,45]. This approach is associated with an artificial thickness of the interface, which is usually set equal to the length of a few computational cells for the best performance. Therefore, fixing the ratio of this smoothing length to the cell size [45], a highly refined mesh is necessary in the vicinity of the interface and the contact-line in order to minimize the error. A remedy to this issue is to utilize a computational mesh that is fitted to the liquid-gas interface, *e.g.* [63,64,46]. However, such an approach may result in severely deformed meshes and requires a frequent remeshing, which dramatically increases the computational costs, particularly in 3D. Moreover, in case of a severe topological change in the liquid phase, this class of approaches may lead to ambiguities in the recognition of the liquid boundary.

In this work, a numerical method is presented that by alleviating the above mentioned issues, provides reasonably accurate results on rather coarse meshes. The previously introduced pressure-enriched finite element/level-set model for the two-phase flows [65] is further developed by incorporating the requirements of the moving contact-line problems. The simplified form of the molecular–kinetic model is implemented along with the Navier-slip condition that acts on the solid substrate. Following the methodology presented by Buscaglia and Ausas [66], the implementation of the moving contact line condition is done by revising the variational formulation of the method. In order to make the overall numerical algorithm consistent, the level-set smoothing procedure [65] is also modified by introducing a boundary condition that is compatible with the contact line condition. To account for the sub-elemental hydrodynamics, the simplified form of Cox's relation [19] is used under the condition of a small capillary number. In addition, this relation is applied only once the contact angle reaches the value within a threshold of the equilibrium contact angle. This ensures that the contact line velocity is limited and consequently, the Reynolds number is small. Nevertheless, in order to remove these limitations, a more general hydrodynamic model [67,54] should be acquired that is a subject of future developments. In this work, an element split-

ting procedure [65] is performed at each step, which enables representing interface with zero-thickness. Consequently, the terms associated with the moving contact-line model are integrated along the curve representing the contact-line while the surface tension acts locally at the interface. It must be noted that such domain splitting is fully exploited by incorporating an enriched finite element space, which enables pressure (gradient) discontinuity within an element.

In the following section, the governing equations including the contact-line condition are first discussed and then implemented in the variational form. Then, the customized version of the level-set method is briefly described and the additional boundary condition required for the smoothing procedure is introduced. The performance of the present method is verified by comparing the result with the theoretical relation between the footprint radius and the contact angle of a droplet spreading with a spherical-cap shape [68] at a small Bond number [69]. The results are further validated against the experimental data published by Seveno et al. [26] for a droplet of liquid squalane that is spreading on a solid silica substrate. The degree of mesh-(in)dependence of the results is shown for both test-cases. All simulations presented in this work are conducted for three-dimensional computation domains.

2. Numerical method

The momentum and mass conservation equations for a fluid system can be written as

$$\rho\left(\frac{\partial \mathbf{u}}{\partial t}+\mathbf{u}\cdot\nabla\mathbf{u}\right)=\rho\mathbf{b}+\nabla\cdot\boldsymbol{\sigma}\quad \text{in } \Omega, \tag{1}$$

and

$$\frac{\partial \rho}{\partial t}+\nabla\cdot(\rho\mathbf{u})=0\quad \text{in } \Omega, \tag{2}$$

respectively. It should be noted that in this work, the homogeneous fluid domains (liquid and gas) are considered to be incompressible and consequently, Eq. (2) reduces to $\nabla\cdot\mathbf{u}=0$ in each phase. The fluid domain, $\Omega\subset\mathbb{R}^d$, is bounded by boundary $\partial\Omega\subset\mathbb{R}^{d-1}$, where d defines the number of spatial dimensions. This set of equations is subject to the initial condition

$$\mathbf{u}(\mathbf{x},0)=\mathbf{u}_0\quad \text{in } \Omega, \tag{3}$$

Dirichlet

$$\mathbf{u}(\mathbf{x},t)=\mathbf{u}_D\quad \text{on } \partial\Omega_D, \tag{4}$$

and Neumann

$$\mathbf{T}(\mathbf{x},t)=\mathbf{T}_N\quad \text{on } \partial\Omega_N, \tag{5}$$

boundary conditions. The traction vector is calculated as $\mathbf{T}=\mathbf{n}\cdot\boldsymbol{\sigma}$ with the total stress tensor, $\boldsymbol{\sigma}$, being obtained from the Newtonian constitutive equation

$$\boldsymbol{\sigma}=-p\mathbb{I}+\mu\left(\nabla\mathbf{u}+\nabla\mathbf{u}^T\right). \tag{6}$$

Here, $\mathbf{n}$ is a unit vector normal to $\partial\Omega$ and pointing to the outside of Ω.

2.1. Multi-phase flow

Let us consider a system consisting of two immiscible fluids and a solid substrate (see Fig. 1). Then, the domain Ω can be separated into Ω_1 and Ω_2 with $\Gamma=(\Omega_1\cap\Omega_2)$ and $\Omega=(\Omega_1\cup\Omega_2)$. The separating interface Γ is a constituent part of both $\partial\Omega_1$ and $\partial\Omega_2$, while it coincides with the solid substrate only at the contact-line $\partial\Gamma=(\partial\Omega\cap\Gamma)$, where the three phases (both fluids 1 and 2 along with the solid substrate) come into contact and three surface tensions, γ, γ_{1s}, and γ_{2s}, act simultaneously on the fluid 1-fluid 2, fluid 1-solid, and fluid 2-solid interfaces, respectively (see Fig. 2).

Being internal to the fluid domain Ω, the interfacial conditions can be interpreted as a jump in the traction due to the surface tension

$$[\![\mathbf{T}(\mathbf{x},t)]\!]=-\gamma\kappa\mathbf{n}_{int}\quad \text{on } \Gamma, \tag{7}$$

and continuity of the velocity field

$$[\![\mathbf{u}(\mathbf{x},t)]\!]=0\quad \text{on } \Gamma, \tag{8}$$

where $\mathbf{n}_{int}$ is the normal to the interface, Γ, and for any variable A the jump operator reads $[\![A]\!]=A_1-A_2$ with subscripts 1 and 2 denoting the value in the corresponding phase domains.

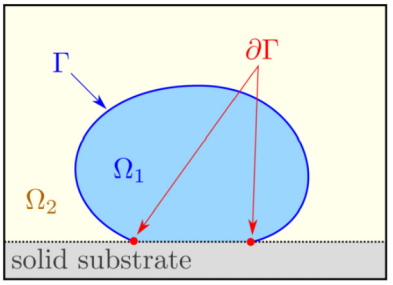

Fig. 1. Schematic of the fluid domain $\Omega = \Omega_1 \cup \Omega_2$.

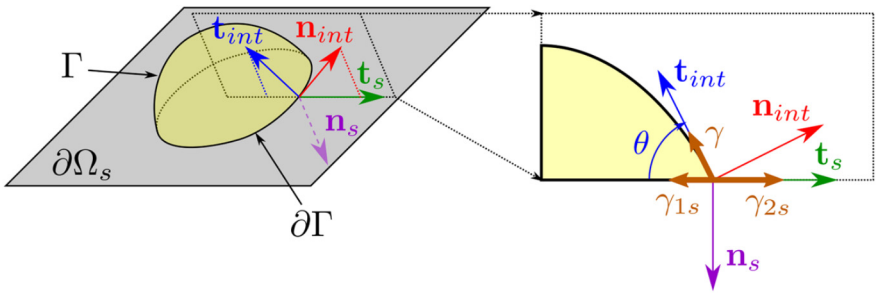

Fig. 2. Schematic of a droplet contacting a solid surface. Liquid-gas, liquid-solid, and gas-solid surface tensions with respective coefficients of γ, γ_{1s}, and γ_{2s} are depicted in this figure.

At the contact–line for the equilibrium state [70] ($\theta = \theta_Y$), Young's relation [71] states that [10,72]

$$\gamma \cos(\theta_Y) + \gamma_{1s} = \gamma_{2s}. \tag{9}$$

Therefore, one can simply write $\cos(\theta_Y) = (\gamma_{2s} - \gamma_{1s})/\gamma$. In case the configuration deviates from the equilibrium, the unbalanced Young stress (force per unit length) is defined as [32,50]

$$\tau_Y = \gamma \left[\cos(\theta_Y) - \cos(\theta)\right]. \tag{10}$$

Here, τ_Y can be interpreted as the net (effective) tension that acts parallel to the solid substrate at the contact-line and is responsible for its movement. Based on the molecular–kinetic theory [21], the movement of the contact-line is associated with an energy dissipation that is usually referred to as a friction force acting on a moving contact-line [33,39,50]. Denoting the slip–velocity associated with the movement of the contact–line with u_{slip}, this underlying mechanism can be represented by [25,36]

$$u_{slip} = 2k^0\lambda \sinh\left(\frac{\lambda^2 \tau_Y}{2k_B T}\right) \quad \text{on } \partial\Gamma, \tag{11}$$

where parameters k^0 and λ are the characteristic frequency and the average distance of the (random thermal) molecular displacements in the vicinity of the contact–line, respectively. In Eq. (11), k_B is the Boltzmann constant and T denotes the absolute temperature. In its simplest form, if the argument of sinh in Eq. (11) is small, the formula of the molecular–kinetic theory reads

$$\tau_Y = \zeta u_{slip} \quad \text{on } \partial\Gamma, \tag{12}$$

with $\zeta = k_B T/k^0\lambda^3$ representing the coefficient of friction at the contact–line [26]. Furthermore, in order to avoid the singularity in the vicinity of the contact-line [73], the no-slip condition on the solid substrate is substituted by the Navier-slip boundary condition that can be formulated as [39,66,74]

$$\mathbf{n}_s \cdot \mathbf{u} = 0 \quad \text{on } \partial\Omega_s, \tag{13}$$

and

$$\mathbb{I}_s \cdot \mathbf{T} = -\beta \mathbb{I}_s \cdot \mathbf{u} = -\beta \mathbf{u} \quad \text{on } \partial\Omega_s, \tag{14}$$

where $\mathbf{n}_s$ is the normal to solid substrate $\partial\Omega_s$, and $\mathbb{I}_s = (\mathbb{I} - \mathbf{n}_s \otimes \mathbf{n}_s)$ denotes the surface unit tensor with $\mathbb{I}$ being the identity tensor. In this work, the slip condition (13) is implemented using the local rotation of the unknown velocities at solid surface $\partial\Omega_s$ as discussed in [75].

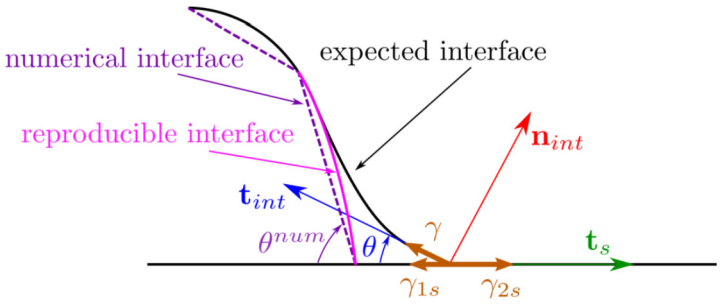

Fig. 3. Schematic of the computationally reproduced and the physically expected interface.

It is worth mentioning that the combination of (12) and (14) is essentially equivalent to the so-called "generalized Navier boundary condition" [39]. Another important point to mention is that so far, no systematic approach has been introduced for *a priori* determination of parameters β and ζ to be used in a numerical simulation [45]. In section 3.2, it is shown that for the present method, ζ can be set according to the corresponding parameter obtained by fitting the experimental data by a comparable model (*e.g.* see [26]).

2.1.1. Sub-element hydrodynamics

Considering the practical difficulties in computationally resolving the hydrodynamics in the vicinity of the contact-line with micrometer length-scales [76,53,77], the well-established hydrodynamic theory is utilized to incorporate the sub-element variation of the contact angle that occurs due to the so-called "viscous bending" phenomenon [25,1] (see Fig. 3). In this work, the formulation is based on the simplified linear form [68] of the asymptotic solution to the hydrodynamic theory [19] as

$$\theta^3 = \left(\theta^{num}\right)^3 - 9\mathrm{Ca}\ln\left(\frac{h_e}{l_{micro}}\right), \tag{15}$$

where the capillary number is defined as $Ca = u_{cl}\mu/\gamma$ and l_{micro} is the microscopic slip length-scale. If h_e is considered to be equal to the length-scale associated with the conventional experimental measurements of the contact-angle, $\ln(h_e/l_{micro}) \sim 10$ would be expected [25,68]. It is worth noting that the simultaneous incorporation of Eqs. (12) and (15) leads to the simplified form of the combined molecular–kinetic/hydrodynamic model proposed by Petrov and Petrov [31,26].

The original Cox's relation [19] is valid for $Ca \ll 1$ and small Reynolds number while its simplified form in Eq. (15) can be utilized in cases of a small contact angle, $\theta < 3\pi/4$, with a vanishing viscosity ratio, $\mu_2/\mu_1 \ll 1$ (considering μ_2 for the surrounding fluid Ω_2) [68]. For the test-cases solved in this paper, Eq. (15) is applied only for $Ca < 0.3$ and $\theta^{num} - \theta_Y < 2\pi/10$. The latter condition prevents the application of Eq. (15) in situations that a large difference between the dynamic contact-angle and θ_Y leads to a rather large contact-line velocity and consequently, a fairly large Reynolds number. In order to alleviate this condition, one can follow the approach presented in [67]; however, in order to keep the simplicity of the formulation, it is not implemented in this work.

Although it is known that the microscopic length-scale l_{micro} is in the order of one nanometer, it is generally obtained by performing a proper data-fitting [26,68]. In this sense, l_{micro} is added to the list of unknown model parameters [35] along with β and ζ. For the cases considered in this work, microscopic length-scale is set to $l_{micro} = 10^{-9}$ m that gives $\ln(h_e/l_{micro}) \sim 10$ for the employed computational meshes. Numerical simulations also show that slight variation of l_{micro} does not lead to any significant changes in the results. Combining Eq. (15) with the generalized Navier condition, Yamamoto et al. has also reported that $l_{micro} \sim 10^{-9}$ m led to the most satisfactory results in their capillary rise simulations [56].

2.2. Variational formulation

The variational form of the momentum equation (1) can be written for the whole fluid domain as [65]

$$\int_\Omega \rho\left(\frac{\partial \mathbf{u}}{\partial t} + \mathbf{u}\cdot\nabla\mathbf{u}\right)\cdot\mathbf{w}d\Omega = \int_\Omega \rho\mathbf{b}\cdot\mathbf{w}d\Omega + \int_\Omega p\nabla\cdot\mathbf{w}d\Omega$$
$$-\int_\Omega \mu\left(\nabla\mathbf{u} + \nabla\mathbf{u}^T\right):\nabla\mathbf{w}d\Omega + \int_{\partial\Omega}\mathbf{T}\cdot\mathbf{w}d(\partial\Omega), \tag{16}$$

where $\mathbf{w}$ is a test function in $\left[\mathcal{H}^1(\Omega)\right]^d$ that vanishes at the Dirichlet boundary conditions. For separate incompressible fluid domains, Ω_1 and Ω_2, the variational form of the continuity equation (2) becomes

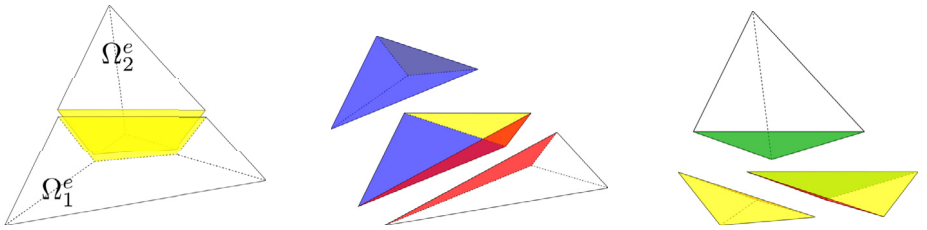

Fig. 4. Schematic of a possible cut in a tetrahedral element. The interface, Γ^e, is shaded by yellow and the matching faces are marked with the same color. (For interpretation of the colors in the figure(s), the reader is referred to the web version of this article.)

$$\int_\Omega q\rho\,(\nabla\cdot\mathbf{u})\,d\Omega = 0, \tag{17}$$

with q being a test-function in $\mathcal{L}^2(\Omega)$. The boundary integral term $\int_{\partial\Omega}\mathbf{T}\cdot\mathbf{w}d(\partial\Omega)$ on the right–hand–side of Eq. (16) essentially includes the Neumann boundary (5), interfacial (7), and Navier-slip (14) conditions as well as the surface tension along with the molecular–kinetic model (11) acting at the contact line. Considering unit vectors $\mathbf{t}_{int}$ and $\mathbf{t}_s$ being tangential to the interface and the solid substrate, respectively (as shown in Fig. 2), one has $\mathbb{I}_s\cdot\mathbf{t}_{int} = -\cos(\theta)\mathbf{t}_s$ and consequently, the molecular–kinetic model (11) can be rewritten as

$$(\gamma_{2s}-\gamma_{1s})\mathbf{t}_s + \gamma\mathbb{I}_s\cdot\mathbf{t}_{int} - \frac{2k_BT}{\lambda^2}\sinh^{-1}\left(\frac{u_{slip}}{2k^0\lambda}\right)\mathbf{t}_s = 0 \quad \text{on } \partial\Gamma. \tag{18}$$

Substituting the corresponding relations into Eq. (16), one obtains

$$\begin{aligned}
\int_\Omega \rho\left(\frac{\partial\mathbf{u}}{\partial t}+\mathbf{u}\cdot\nabla\mathbf{u}\right)\cdot\mathbf{w}d\Omega &= \int_\Omega \rho\mathbf{b}\cdot\mathbf{w}d\Omega + \int_\Omega p\nabla\cdot\mathbf{w}d\Omega \\
&- \int_\Omega \mu\left(\nabla\mathbf{u}+\nabla\mathbf{u}^T\right):\nabla\mathbf{w}d\Omega + \int_{\partial\Omega_N}\mathbf{T}_N\cdot\mathbf{w}d(\partial\Omega) \\
&- \int_{\partial\Omega_s}\beta\mathbf{u}\cdot\mathbf{w}d(\partial\Omega) - \int_\Gamma \gamma\kappa\mathbf{n}_{int}\cdot\mathbf{w}d\Gamma \\
&+ \int_{\partial\Gamma}\Big[(\gamma_{2s}-\gamma_{1s})\mathbf{t}_s + \gamma\mathbb{I}_s\cdot\mathbf{t}_{int} \\
&- \frac{2k_BT}{\lambda^2}\sinh^{-1}\left(\frac{u_{slip}}{2k^0\lambda}\right)\mathbf{t}_s\Big]\cdot\mathbf{w}d(\partial\Gamma).
\end{aligned} \tag{19}$$

Here, the slip–velocity at the contact–line reads $u_{slip} = \mathbf{t}_s\cdot\mathbf{u}$. Simplifying the molecular–kinetic model (11) to its linear form (12), one obtains

$$\int_{\partial\Gamma}\frac{2k_BT}{\lambda^2}\sinh^{-1}\left(\frac{u_{slip}}{2k^0\lambda}\right)\mathbf{t}_s\cdot\mathbf{w}d(\partial\Gamma) = \int_{\partial\Gamma}\zeta(\mathbf{t}_s\cdot\mathbf{u})\mathbf{t}_s\cdot\mathbf{w}d(\partial\Gamma). \tag{20}$$

For the sake of simplicity and in order to facilitate comparisons with the references chosen in the present work (where ζ is provided), the linear approximation (Eq. (20)) is used if not mentioned otherwise.

It must be noted that a similar variational formulation for the contact line dynamics has been derived by Buscaglia and Ausas [66] using the principle of virtual work. Conventionally, the variational formulation is derived by smoothing the surface tensions based on the continuum force approach (see [42] for example).

In this work, the accurate integration of the terms appearing in the variational formulation (19) is done by splitting of the cut elements. In Fig. 4, this procedure is schematically shown for a sample element cut by the interface. Elemental integration domains $\Omega_1^{e,cut}$ and $\Omega_2^{e,cut}$ are split into tetrahedra to facilitate the integration. The integration of the terms associated with the elemental interface (Γ^e), contact-line ($\partial\Gamma^e$), and solid substrate ($\partial\Omega_s^e$) are performed by utilizing the quadrature points as schematically illustrated in Fig. 5. By employing a high–order (two points for line-segments, three points for triangles, and four points for tetrahedra) Gaussian quadrature, one can assure that the integration procedure does not introduce further error to the solution (*i.e.* the number of Gauss points is sufficient for the integration of functions up to third–order). The conventional alternative to the element splitting procedure is the incorporation of a smoothed numerical

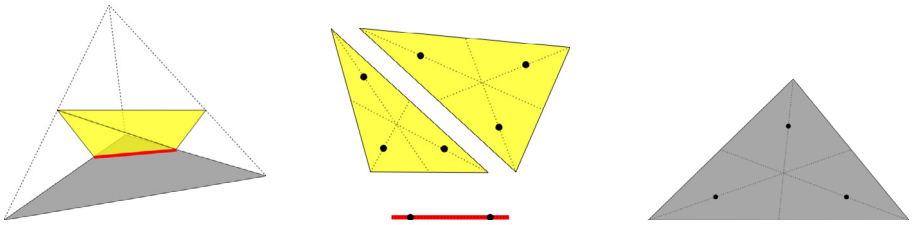

Fig. 5. Schematic of a possible cut in a tetrahedral element contacting the solid surface. $\partial\Gamma^e$ is marked with a red solid line and quadrature points are represented by black dots.

approximation of the delta function; in the continuum force approach, this is essentially needed to formulate the surface tension and the contact–line model. In the present approach, due to the employment of the splitting methodology, such an approximation is not required and the associated errors are alleviated.

The presented formulation is implemented withing the framework of the stabilized pressure enriched finite element method proposed in [65]. Within element e, the standard finite element approximation of the flow variables reads

$$\mathbf{u}(\mathbf{x},t) = \sum_{I\in\mathcal{N}^e} \mathbf{u}_I(t) N_I^e(\mathbf{x}), \tag{21}$$

and

$$p(\mathbf{x},t) = \sum_{I\in\mathcal{N}^e} p_I(t) N_I^e(\mathbf{x}), \tag{22}$$

where $\mathcal{N}^e$ denotes the set of associated nodes and N_I^e is the shape function corresponding to node I. However, using the standard finite element approximation, it is impossible to capture the intra-element discontinuity in the presence of material interfaces; in the context of multi-phase flows [65], this is the source of the so-called "spurious currents". In order to resolve this issue, the pressure approximation within an element cut by the interface can be enriched by accounting for a "jump" as

$$p(\mathbf{x},t) = \sum_{I\in\mathcal{N}^{e,cut}} p_I(t) N_I^{e,cut}(\mathbf{x}) + \sum_{I\in\mathcal{N}^{e,cut}} p_{I,enr}^{e,cut}(t) N_{I,enr}^{e,cut}(\mathbf{x}), \tag{23}$$

with enriched nodal pressure $p_{I,enr}^{e,cut}$ being local to the cut element.

In this work, enriched shape function $N_{I,enr}$ is constructed based on standard continuous shape function N_I as

$$N_{I,enr}(\mathbf{x}) = \begin{cases} N_I(\mathbf{x}) & \textbf{if } (\mathbf{x}_I \in \Omega_1 \textbf{ and } \mathbf{x} \in \Omega_2) \textbf{ or } (\mathbf{x}_I \in \Omega_2 \textbf{ and } \mathbf{x} \in \Omega_1) \\ 0 & \textbf{else} \end{cases} \tag{24}$$

Using this set of enriched shape functions, both the jump in the pressure and discontinuity in its gradient can be captured within a cut element. After introducing the enrichment terms, the variational multiscale methodology with the well–established algebraic sub-grid scale stabilization [78] along with a special small–cut treatment approach is utilized to stabilize the method as proposed in [65]. The momentum equation is then linearized using the generalized Newton's method and solved along with the mass conservation equation in a fully implicit monolithic manner. One of the remarkable features of this enrichment procedure is that upon the creation of the local elemental system of equations, pressure condensation procedure [65] is performed at the elemental level, thus, omitting the introduction of the additional enriched pressure degrees of freedom. Therefore, the degrees of freedom, and consequently, the size of the assembled global system of equations is the same as that of the standard finite element method.

2.3. Level-set

In the present method, the evolution of the interface is captured using the level-set method [79], which is based on the introduction of the continuous function ϕ that represents the signed distance to the interface. The level-set function is convected according to the velocity field by solving

$$\frac{\partial\phi}{\partial t} + \mathbf{u}\cdot\nabla\phi = 0 \quad \text{in } \Omega. \tag{25}$$

In the present work, this pure convection equation is stabilized following the methodology proposed by Codina [80]. The level-set function gradually loses its regularity due to its deviation from a distance function [81] and high frequency noise

(oscillatory interface) [82]. The first problem can be resolved by frequent reinitialization of the level-set function in a way that $\|\nabla\phi\| \approx 1$ is satisfied [83]. Due to the hyperbolic nature of the conventional level-set reinitialization formulation, it is necessary to take into account the so-called "blind-spot region" in the vicinity of the solid surface [84]. Nonetheless, in the present work, the marching level-set reinitialization procedure proposed by Elias et al. [85] is performed for the whole domain once in every 50 time-steps.

Following the idea presented in [86], the high frequency oscillations can be effectively cured by solving a diffusion equation for the level-set function as

$$\tilde{\phi} - \varepsilon\nabla^2\tilde{\phi} = \phi \quad \text{in } \Omega, \tag{26}$$

where $\tilde{\phi}$ and ϕ are the smoothed (non-oscillatory) and original level-set functions, respectively. Here, $\varepsilon = 5\times10^3\Delta t h_e^2$, with Δt being the size of the time-step and h_e the element size. In the absence of contact with a solid, Eq. (26) can be solved without introducing any specific boundary condition [86,82,65]. In the present method, a Neumann boundary condition is implemented on the solid substrate as

$$\mathbf{n}_s \cdot \nabla\tilde{\phi} = \mathbf{n}_s \cdot \nabla\phi \quad \text{on } \partial\Omega_s. \tag{27}$$

Combining Eqs. (10), (12), and (15),

$$\theta^{num} = \left\{ \left(\cos^{-1}\left[\frac{\zeta}{\gamma} u_{slip} + \cos(\theta_Y) \right] \right)^3 + 9\mathrm{Ca}\ln\left(\frac{h_e}{l_{micro}}\right) \right\}^{1/3}, \tag{28}$$

at the cut elements, boundary condition (27) is substituted by

$$\mathbf{n}_s \cdot \nabla\tilde{\phi} = -\|\nabla\phi\|\cos(\theta^{num}) \quad \text{on } \partial\Omega_s^{e,cut}. \tag{29}$$

It should be noted that in case of the application of the full form of the molecular–kinetic model, Eq. (28) should be rewritten incorporating Eq. (11).

The main shortcoming of the presented level-set smoothing scheme is the probability of a slight droplet shrinkage. As proposed in [65], this issue can be resolved by performing a correction step as

$$\phi_I = \tilde{\phi}_I - \frac{1}{\mathcal{N}_I}\sum_J^{\mathcal{N}_I}\left(\tilde{\phi}_J - \phi_J\right), \tag{30}$$

where $\mathcal{N}_I$ is the number of nodes J that are connected to node I. In this work, in order not to perturb the contact angle, a modified correction procedure is proposed by separating the set of nodes interior to the fluid domain from those that lie on the solid substrate, *i.e.*

$$J \in \begin{cases} \Omega \setminus \partial\Omega_s & \text{if } I \in (\Omega \setminus \partial\Omega_s) \\ \partial\Omega_s & \text{if } I \in \partial\Omega_s \end{cases} \tag{31}$$

Above, all the ingredients of the proposed method are detailed. The summary of the overall strategy is presented in Algorithm 1.

3. Results

The proposed numerical method is implemented within KRATOS Multiphysics [87] an open-source framework for multi-physics computations. The second order backward difference (BDF2) time integration is applied to the flow equations and the Crank–Nicolson scheme is used for time-marching of the level-set convection equation. Algebraic multigrid library (AMGCL [88]) was used to solve the linear system of equations using the GMRES(m) method (with restart parameter $m = 40$). The convergence tolerance of the linear solver is set to 10^{-9}, while a relative tolerance of 10^{-5} is considered to check the convergence of velocity and pressure.

In the following, the performance of proposed numerical method is first verified by comparing the simulation results with the theoretical relation obtained for the footprint radius of a liquid droplet spreading on a solid substrate at small Bond numbers. The method is further validated against the experimental data published in the literature for a millimeter-sized squalane droplet spreading on a substrate of silicone wafer. In the end, the capability of the method is assessed by simulating a droplet trapped inside conical pores. In all cases solved in this paper, gravity $g = 9.8$ m/s^2 acts in the negative z–direction, and Ω_2 is composed of air with $\rho = 1.0$ kg/m^3 and $\mu = 1.0\times10^{-5}$ Pa s. For the sake of convenience, the contact-angle is reported in degrees in the rest of this paper.

Remark. Before assessing the results of the proposed method, it is worth to provide an insight of the computational costs associated with its application: using a mesh with ~ 500 K elements, the total run–time per time–step is around 62 s, of which almost 80% corresponds to the two-phase flow solver, 4% to the level–set convection, 8% to the level–set smoothing procedure, and about 8% is consumed for the level–set re-initialization procedure.

Algorithm 1: Summary of the proposed method.

Input: $\mathbf{u}_0$, $\mathbf{u}_D$, $\mathbf{T}_N$, and ϕ_0
Output: $\mathbf{u}_I$, p_I, and ϕ_I; node $I \in \Omega$

```
n = 1
t = 0
while t < run-time do
    solve Eq. (25) for φ_I^(n+1/2) with half time-step
    if n = {50, 100, 150, ...} then
        reinitialize φ
    do smoothing according to Eqs. (26) and (30) with conditions (27) and (29)
    calculate curvature
    for all elements e do
        if e ∩ Γ ≠ ∅ then
            do element splitting
            calculate contact angle
        create elemental system of equations
    do assembling the Linear System of Equations (LSE)
    solve LSE for [u_I^(n+1), p_I^(n+1)]
    solve Eq. (25) for φ_I^(n+1) with half time-step
    update n = n + 1
    update t = nΔt
```

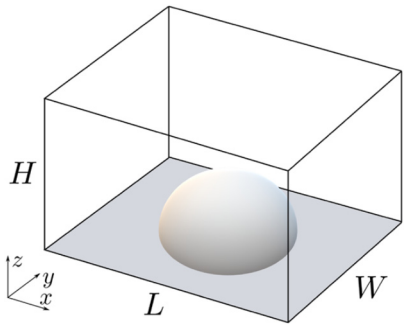

Fig. 6. Schematic of the initial configuration of the liquid droplet inside a solid box.

3.1. Verification with theory

If a droplet retains its spherical-cap shape during spreading on a solid surface, one can write a correlation between the footprint radius and the instantaneous contact-angle based on the mass conservation of an incompressible liquid. The resulting correlation reads as $r(t) = f(\theta(t))$ with [33]

$$f(\theta) = \left\{ \frac{3V}{\pi} \frac{[1+\cos(\theta)]\sin(\theta)}{[1-\cos(\theta)][2+\cos(\theta)]} \right\}^{1/3}. \tag{32}$$

Starting from $\theta(0) = \pi/2$, the ratio of the terminal radius r_Y to the initial radius of the droplet R_0 is

$$\frac{r_Y}{R_0} = \left\{ \frac{2[1+\cos(\theta_Y)]\sin(\theta_Y)}{[1-\cos(\theta_Y)][2+\cos(\theta_Y)]} \right\}^{1/3}. \tag{33}$$

The basic assumption of a spherical-cap droplet is valid if the Bond number ($Bo = \rho_1 g R_0^2/\gamma$) is small or equivalently the height of the droplet is smaller than the capillary length-scale ($l_c \sim \sqrt{\gamma/\rho_1 g}$) [69,33,68]. This condition indicates that gravity is dominated by the capillary force and therefore, has a negligible effect on the droplet dynamics. Note that this assumption is questionable for fluids with large viscosity, *e.g.* for polymeric liquids [33].

Here, a liquid droplet with an initially hemispherical shape (initial contact-angle of $\theta_0 = 90°$) and an initial radius of $R_0 = 1.5$ mm is spreading on a solid substrate. The system is confined in a box filled by air with no-slip lateral and top boundaries. The schematic of the whole system is shown in Fig. 6. The dimensions are $L = W = 8$ mm and $H = 3$ mm, liquid viscosity is $\mu_1 = 1.0 \times 10^{-3}$ Pa s, density is $\rho_1 = 920$ kg/m^3, and the liquid-air surface tension is $\gamma = 4.26 \times 10^{-2}$ N/m. This gives a $Bo = 0.48$ or equivalently a capillary length-scale of $l_c = 2.2$ mm. The equilibrium contact-angle is set to $\theta_Y = 58°$ and the results are obtained using $\beta = 10^3$ Pa s/m and $\zeta = 1.0$ Pa s, noting that this example does not intent to reproduce any real-world experiment.

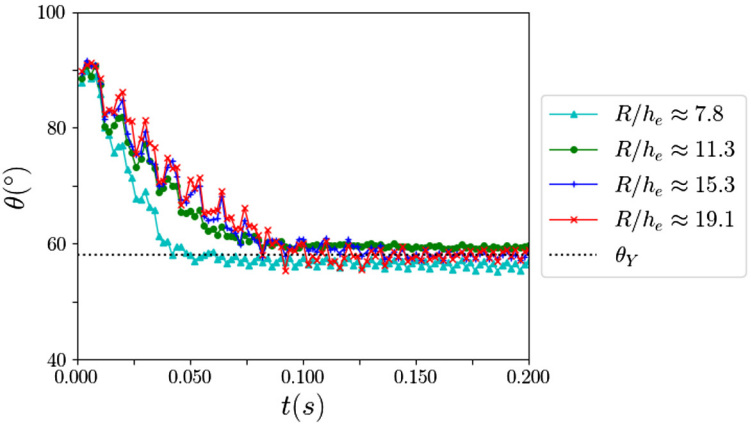

Fig. 7. The effect of the mesh resolution on the time-evolution of the contact angle for a droplet spreading with $Bo = 0.48$ and $\theta_Y = 58°$.

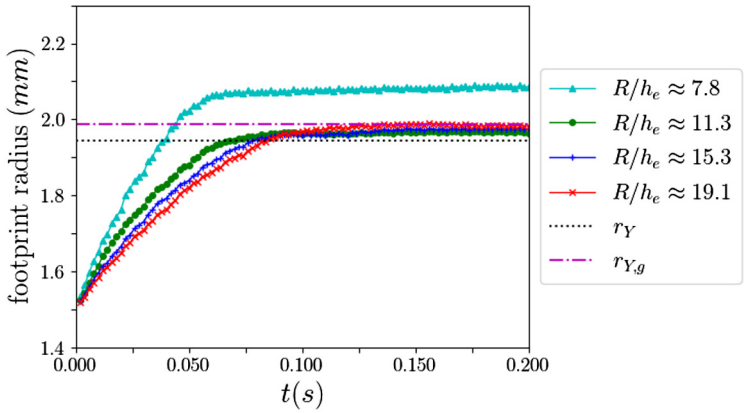

Fig. 8. The effect of the mesh resolution on the time-evolution of the footprint radius of a droplet spreading with $Bo = 0.48$ and $\theta_Y = 58°$.

This problem is solved for four different (structured) meshes of $R_0/h_e \approx 7.8$, 11.3, 15.3, and 19.1, composed of tetrahedral elements with the size of $h_e = (1/6V_e)^{1/3}$, where V_e is the volume of a single element. The time evolution of the contact angle and the footprint (base) radius of the droplet is shown in Figs. 7 and 8, respectively. In this work, the contact-angle is calculated as the average of θ obtained for all cut elements with $\Omega^e \cap \partial\Gamma \neq \varnothing$. The reported radius is also the average distance of the center of the solid substrate, located at $(x, y, z) = (L/2, W/2, 0)$, to the center of all $\partial\Gamma^e = \Omega^e \cap \partial\Gamma$. In the mentioned figures, the theoretical values of θ_Y and r_Y obtained from Eq. (33) are shown for comparison. In addition, since the Bond number is finite, the corrected equilibrium footprint radius, in the presence of gravity is calculated based on the theory developed in [69] and denoted by $r_{Y,g}$ in the following figures.

As seen in Figs. 7 and 8, numerically obtained droplet configuration at equilibrium, *i.e.* (θ_{eq}, r_{eq}) shows a good consistency with the theoretical prediction $(\theta_Y, r_{Y,g})$; while the error in θ_{eq} is around 3.1% and 2.4% for $R_0/h_e \approx 7.8$ and 11.3, respectively, it is reduced to below 0.5% for two finer meshes of $R_0/h_e \approx 15.3$ and 19.1. The corresponding errors in the footprint radius at equilibrium in comparison with $r_{Y,g}$ are around 5.0%, 1.1%, 0.6%, and 0.3% for $R_0/h_e \approx 7.8$, 11.3, 15.3, and 19.1, respectively.

For all the employed meshes, the largest deviation from the theoretical value in terms of the dynamic contact-angle and the evolving footprint radius of the droplet, is observed in the middle stages of the spreading. The mesh-convergence of r_{eq} is shown in Fig. 9. The equilibrium configuration of the droplet is obviously converging by increasing the mesh resolution. In the present test-case, the settings lead to a very small capillary number and therefore, the difference between θ and θ^{num} is fairly small.

Considering the initial configuration of the droplet and fact that the height of the droplet, and consequently the effect of gravity is constantly decreasing during the spreading, it is expected that the spherical-cap assumption and consequently, Eq. (32) can also be applied to the evolution of the radius of the droplet. It is shown in Fig. 10, where the numerically obtained footprint radius of the droplet for $R_0/h_e \approx 15.3$ is compared to Eq. (32); the agreement is clearly seen. However, specially for the initial stages of the spreading, the slight deviation is expected as a result of a finite gravity and the effect of inertia.

It should be noted that releasing the droplet from rest with its center-of-gravity initially located above the solid substrate, triggers a series of oscillations in the contact-angle (see Fig. 7, it is also directly reflected in Fig. 10 for $r = f(\theta)$ curve). These

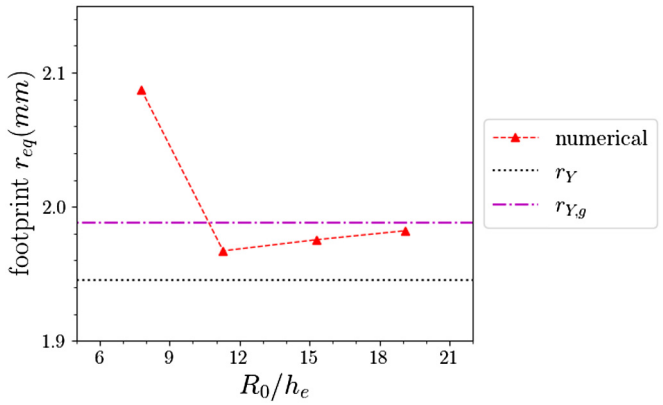

Fig. 9. Mesh convergence of the footprint radius of a droplet spreading with $Bo = 0.48$ and $\theta_Y = 58°$. The theoretical value of r_{eq} is shown by dotted-line.

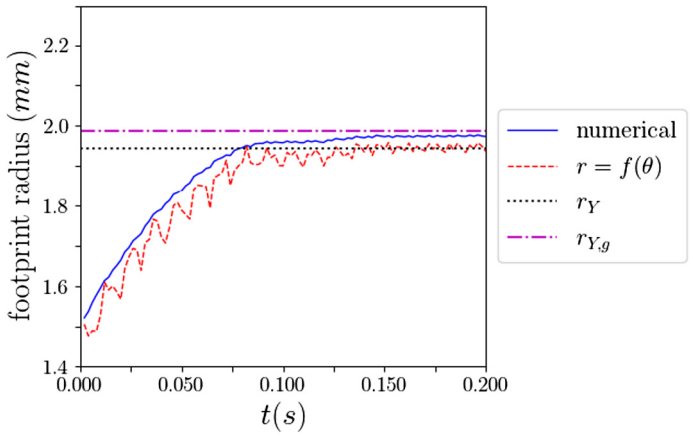

Fig. 10. Time-evolution of the footprint radius of a droplet spreading with $Bo = 0.48$ and $\theta_Y = 58°$, in comparison with $r = f(\theta)$.

are physically expected inertial oscillations with an origin similar to what was theoretically formulated in [89] (art. 275); any disturbance in the shape of a droplet in the simultaneous presence of the surface tension and inertia, results in an oscillatory behavior. Since the initial triggering disturbance is of a spontaneous nature, these oscillations are eventually damped due to viscous dissipation. On the other hand, the persistent high-frequency oscillations of insignificant amplitude in the contact-angle (particularly evident near the steady-state) occur due to the intermittent level-set re-initialization (performed every 50 time–steps in the present work).

3.1.1. Obtuse contact–angle

In order to further analyze the performance of the proposed method for an obtuse equilibrium contact–angle, the same test–case of the droplet spreading is simulated here with $\theta_0 = 159°$ and $\theta_Y = 105°$. Time–evolution of the contact–angle as well as the footprint radius is shown in Fig. 11. Here, despite being characterized by the same Bond number ($Bo = 0.48$), which corresponds to the initial radius of the droplet, the significantly larger height suggests a pronounced effect of gravity on the equilibrium shape of the droplet. This explains the rather large difference between $r_Y = 1.30$ mm and $r_{Y,g} = 1.77$ mm. In addition, releasing the droplet with its center–of–gravity being initially positioned farther from the solid substrate (at $z_0 = 1.4$ mm) triggers more profound inertial oscillations.

The above-presented results show that the present numerical model can successfully capture the configuration of a spreading droplet consistently with the theoretical predictions.

3.2. Validation against experimental data

Next, the proposed numerical method is validated by simulating the spreading of a liquid (squalane) droplet on a solid (silicone wafer) substrate and comparing the obtained numerical results with the experimental data reported in [26]. In this test, besides the time-evolution of the configuration of the droplet at the near-equilibrium stage, the initial stage of the droplet spreading (in which inertia also plays an important role) is taken into account. Therefore, this test allows for the in-depth validation of the proposed numerical method.

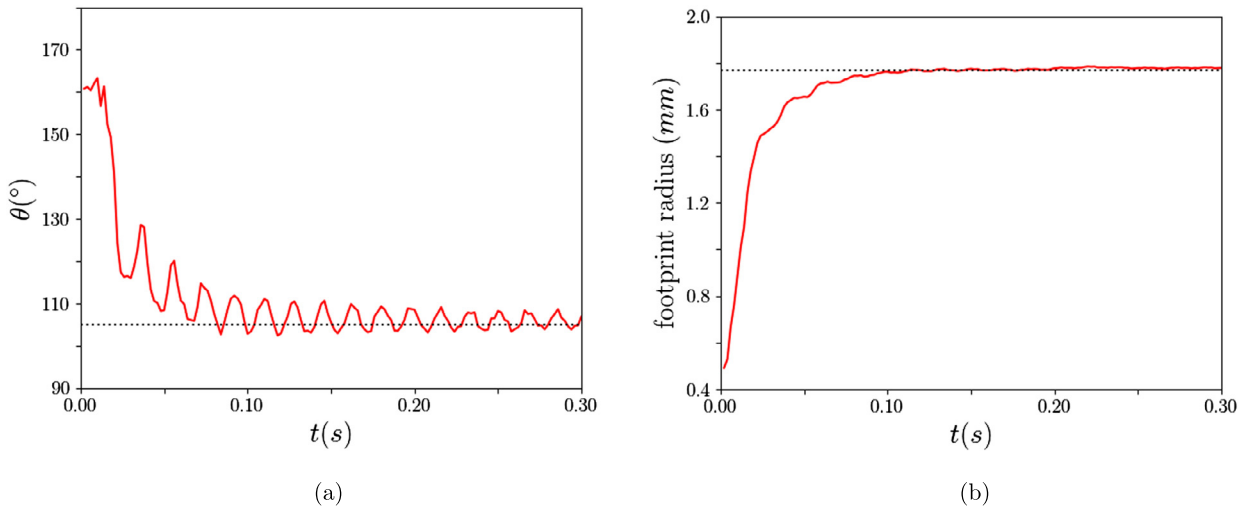

Fig. 11. Time-evolution of (a) the contact–angle and (b) the footprint radius of a droplet spreading with $Bo = 0.48$ and $\theta_Y = 105°$. The solid red line and the dotted line correspond to the numerical result and the theoretical prediction $(\theta_Y, r_{Y,g})$, respectively.

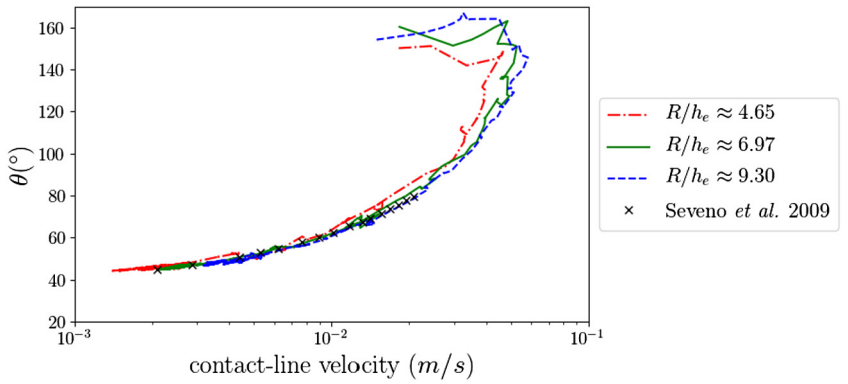

Fig. 12. Contact-angle as a function of the velocity of the contact-line; comparison of the experiment [26] with the numerical data obtained for structured meshes of different resolutions.

Squalane has a viscosity of $\mu_1 = 3.14 \times 10^{-2}$ Pa s, density $\rho_1 = 810$ kg/m^3, and the liquid-air surface tension $\gamma = 3.11 \times 10^{-2}$ N/m. The squalane droplet in contact with the surrounding air and the silicone wafer substrate creates an equilibrium contact angle of 38.8°. Same computational domain as the one used in section 3.1 is chosen (see Fig. 6), while the initial radius and contact-angle of the droplet are set to $R_0 = 0.9$ mm and $\theta_0 = 180°$, respectively. Here, ζ is set to 0.7 Pa s in order to correspond to the value calculated in [26] by performing a data fitting based on the linear Petrov model. The Navier-slip coefficient of $\beta = 10^3$ Pa s/m is chosen so to provide the best match with the experimentally obtained contact velocity-angle relation as shown in Fig. 12. It is observed that the experimental data can perfectly be reproduced by the implemented model for the moving contact-line. Numerical data are obtained by performing simulations on three different structured meshes of tetrahedral elements with $R_0/h_e \approx 4.65$, 6.97, and 9.30. Varying the mesh resolution has a negligible effect on the contact velocity-angle relation.

In Fig. 13, the experimentally obtained time-evolution of the contact-angle is compared to the numerical value for different mesh resolutions. Numerical results are in a good agreement with the experimental data. Mesh-convergence of the solution is confirmed by comparing the results obtained for $R_0/h_e \approx 6.97$, and 9.30. The mesh-convergence is further shown in Fig. 14 for the footprint radius of the droplet during the spreading.

In an attempt to compare the radius of the droplet with data reported in [26], correlation $R = r/\cos(\theta - \pi/2)$ is applied to the numerical data. This correlation, based on the assumption that the spreading droplet has a spherical-cap shape, is valid in the current test-case only during the final stage of the spreading, for which $\theta < 70°$ [26]. Fig. 15 illustrates the reproduced radius of the droplet for different mesh resolutions in comparison with the experimental data.

Upon validation of the proposed method, in the following, the performance of the method is investigated for the same test is simulated on an unstructured mesh. The initial radius to (average) element size ratio of $R_0/h_e \approx 9$ is set for the elements located on the solid surface, *i.e.* $\Omega^e \cap \Omega_s \neq \varnothing$, while the mesh resolution is significantly coarser for internal elements with $R_0/h_e \approx 4.5$. Keeping parameters β and ζ unchanged, the numerically obtained contact velocity-angle relation

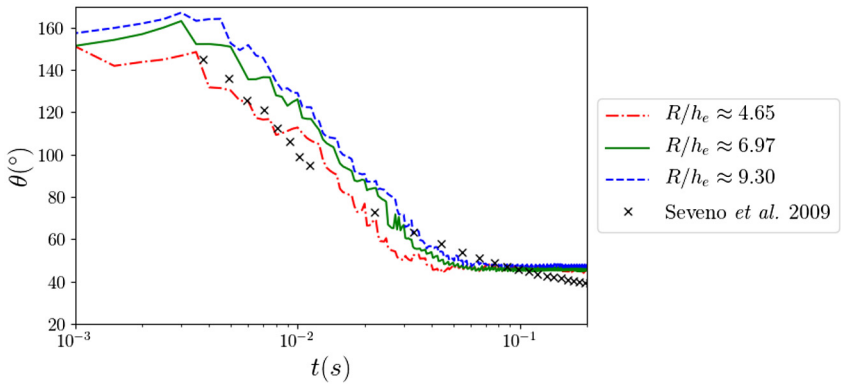

Fig. 13. Time evolution of the contact-angle; comparison of the experiment [26] with the numerical data obtained for structured meshes of different resolutions.

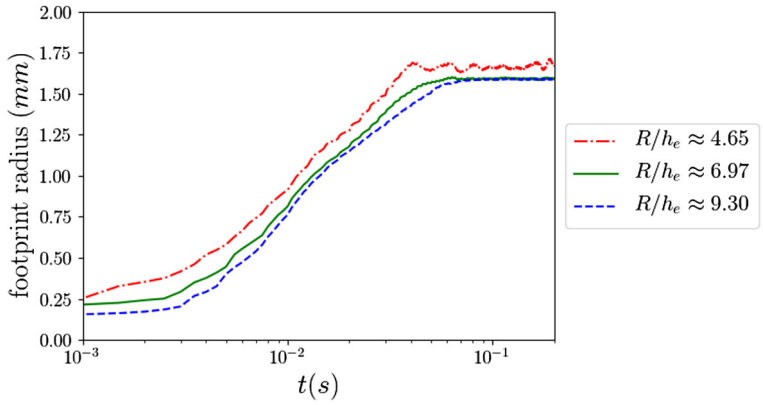

Fig. 14. Time evolution of the footprint radius; comparison of data obtained for structured meshes of different resolutions.

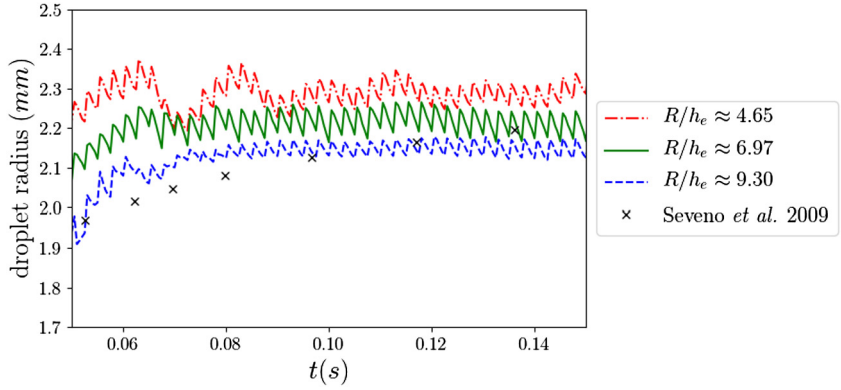

Fig. 15. Radius of the droplet; comparison of the data presented in [26] with the numerical data obtained for structured meshes of different resolutions.

is shown in Fig. 16. Despite a slight deviation, the result is completely satisfactory. The time-evolution of the contact-angle obtained for the unstructured mesh is shown in Fig. 17. The result obtained on the unstructured mesh shows a slight increase in the high-frequency oscillations comparing to that of the structured mesh during the middle stage of the droplet spreading. In order to explore the pressure field, the computational domain is evenly divided and the pressure contours are plotted on the division plane in Fig. 18. The results obtained on structured and unstructured meshes exhibit a good match. The isometric (three-dimensional) and side view of the droplet-air interface is presented in Fig. 19 at different instances. These are obtained by plotting the zero level-set ($\phi = 0$) iso-surfaces obtained for the unstructured mesh. As seen in Figs. 19(g) and 19(h), the deviation from the spherical-cap shape is evident for the initial stage of the spreading.

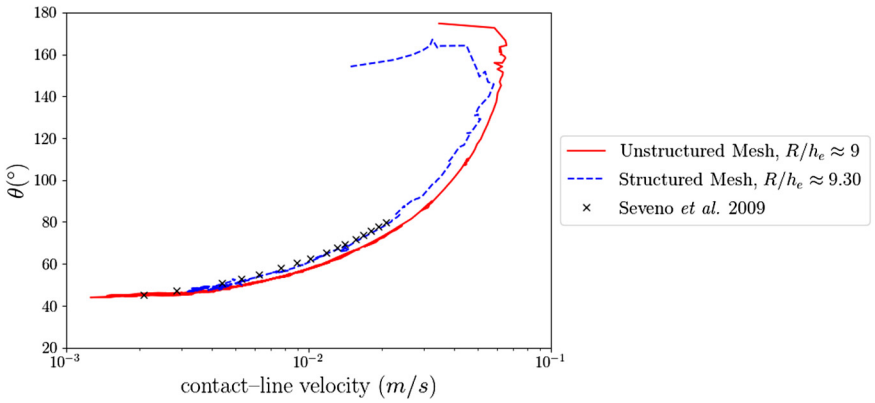

Fig. 16. Contact-angle as a function of the velocity of the contact-line; comparison between the experimental data [26] and the numerical results obtained for the structured and the unstructured meshes.

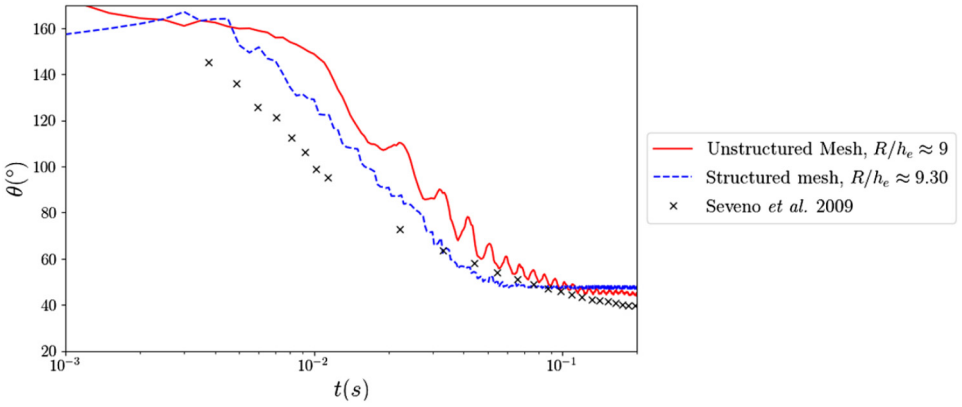

Fig. 17. Time evolution of the contact-angle; comparison between the experimental data [26] and the numerical results obtained for the structured and the unstructured meshes.

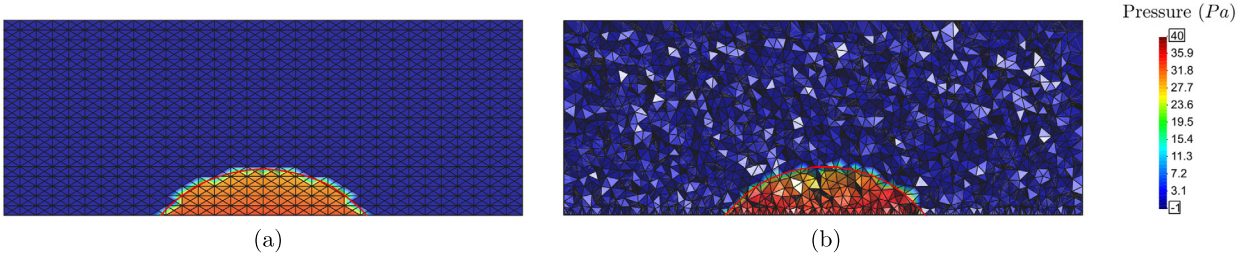

Fig. 18. Pressure contours obtained at $t = 0.1s$ for (a) structured and (b) unstructured meshes.

3.3. Droplet trapped in conical pores

In order to assess the capability of the proposed method in a more complex case, in the following the numerical method is applied to the evolution of a droplet trapped inside conical pores. The settings of this test-case preclude the straightforward application of the conventional schemes, which are basically developed for structured meshes.

The schematic of the configuration of the pore with the initially spherical droplet of radius $R_0 = 0.9$ mm in tangential contact with the cone is shown in Fig. 20. Physical parameters are set according to data reported in section 3.2 for the squalane droplet on the silicone wafer substrate. Here, the simulations are performed for two conical pores of $\alpha = 30°$ and $60°$ with $H = 5.5$ mm and 4 mm, respectively. The computational domain is discretized with tetrahedral elements of size $R_0/h_e \approx 14.3$ adjacent to the solid surface and $R_0/h_e \approx 9$ inside the domain.

The evolution of the trapped droplet is shown in Fig. 21 for $\alpha = 30°$. Starting from a perfectly spherical shape, concave interfaces are gradually established due to $\theta_Y < \pi/2$. As shown in Fig. 22, this leads to a reduced (negative) pressure inside the droplet at equilibrium. Figs. 22 and 23 present the pressure contours inside the computational domain obtained at different time-instances for $\alpha = 30°$ and $60°$, respectively. It is evident that by evolving the interface from a convex to

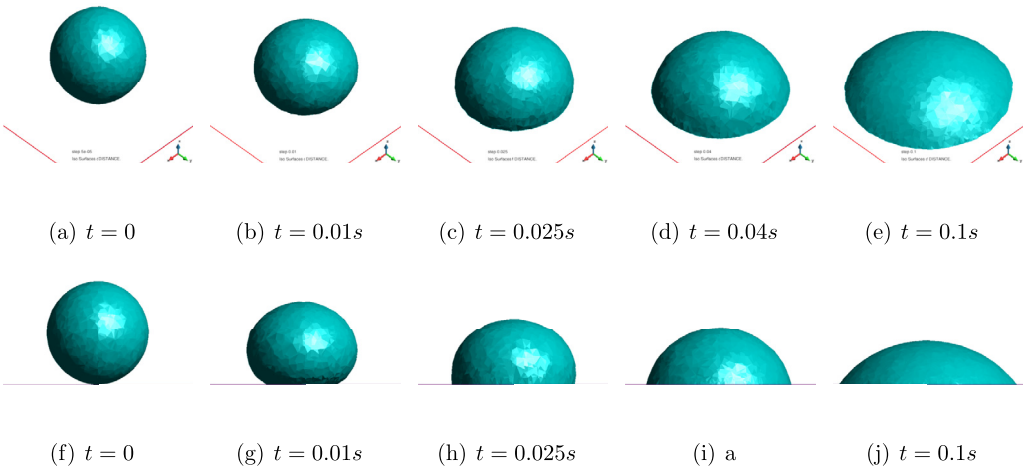

Fig. 19. Evolution of the liquid-air interface of the squalane droplet spreading on silicone wafer.

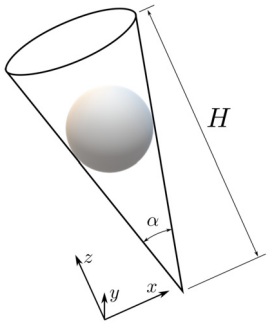

Fig. 20. Schematic of the initial configuration of the droplet trapped in a conical pore.

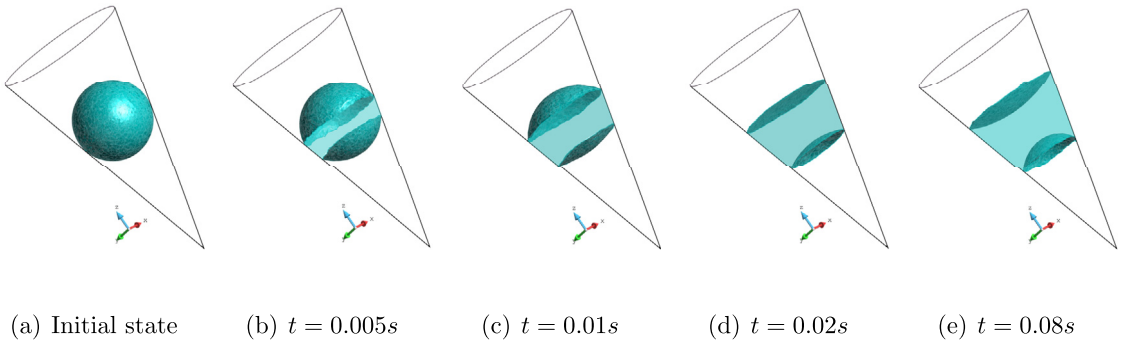

Fig. 21. Evolution of the liquid-air interface of the droplet trapped inside a conical pore with $\alpha = 30°$.

a concave shape, pressure inside the droplet varies from the maximum to the minimum value. The average value of the numerically obtained terminal contact-angle is $\theta_{eq} \approx 43.3°$ for $\alpha = 30°$, and $\theta_{eq} \approx 43.9°$ for $\alpha = 60°$; this is consistent with $\theta_Y = 38.8°$ set as an input parameter for simulations.

The present set of test-cases required, on average, three to four iterations to reach pressure and velocity convergence in each time-step, while the linear solver fulfilled the maximum tolerance condition in about 50 iterations.

4. Summary and conclusion

In order to develop a level-set/enriched finite element method with the capability of treating dynamics of the moving contact-line, a systematic and physically consistent methodology was proposed; the role of the molecular–kinetic theory and the hydrodynamic theory in the numerical modeling were elaborated along with the necessary customization of the boundary conditions including the contact–line dynamics. By applying the proposed method to the spreading of a droplet,

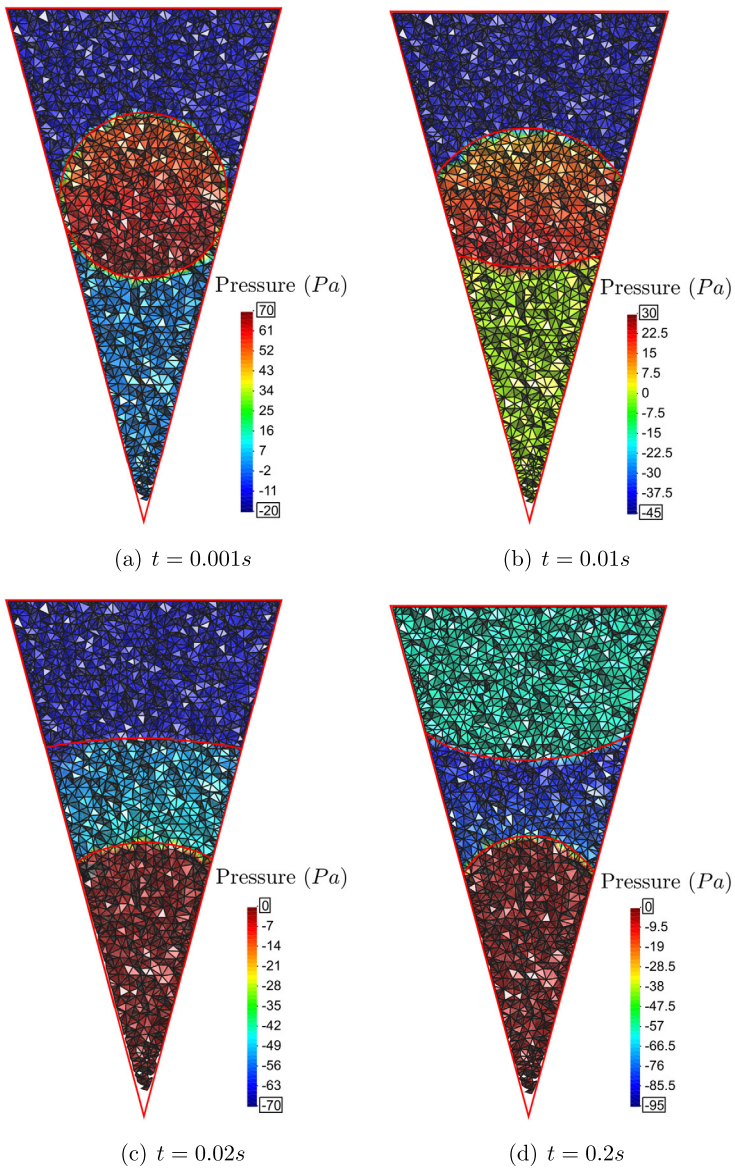

(a) $t = 0.001s$ (b) $t = 0.01s$

(c) $t = 0.02s$ (d) $t = 0.2s$

Fig. 22. Pressure contours for $\alpha = 30°$. At $t = 0.2s$, the system has almost reached its equilibrium configuration.

an acceptable mesh-convergence was observed. The results were also compared for both the structured and unstructured meshes and a good agreement was revealed. Furthermore, the straightforward employment of the proposed method to simulate a droplet trapped in a (closed) conical pore, suggests the applicability of the developed numerical tool for pore-scale multi-phase flows. It must be noted that in this work no mesh-refinement strategy was utilized to locally increase the resolution close to the droplet interface.

One of the interesting features of the present method was that in order to obtain physically meaningful results, the contact-line dissipation coefficient was set according to the corresponding parameter that was obtained by fitting the linear Petrov's model into the experimental data. This alleviates the ambiguity associated with the setting of this parameter in the approaches rely on the generalized Navier-slip condition. However, further investigation with a wider range of liquid/solid materials is necessary to further support this affirmation, which would be the topic of a separate research.

Generally, during the initial stage of the droplet spreading, inertial effects are rather significant and therefore, the validity of the simplified model used in the present work to resolve the sub-elemental hydrodynamics becomes dubious. Therefore, in order to increase the accuracy while capturing the spreading with a finite inertia, a more sophisticated hydrodynamic model that also incorporates the terms appearing at finite Reynolds number can be acquired. This is a subject for future developments.

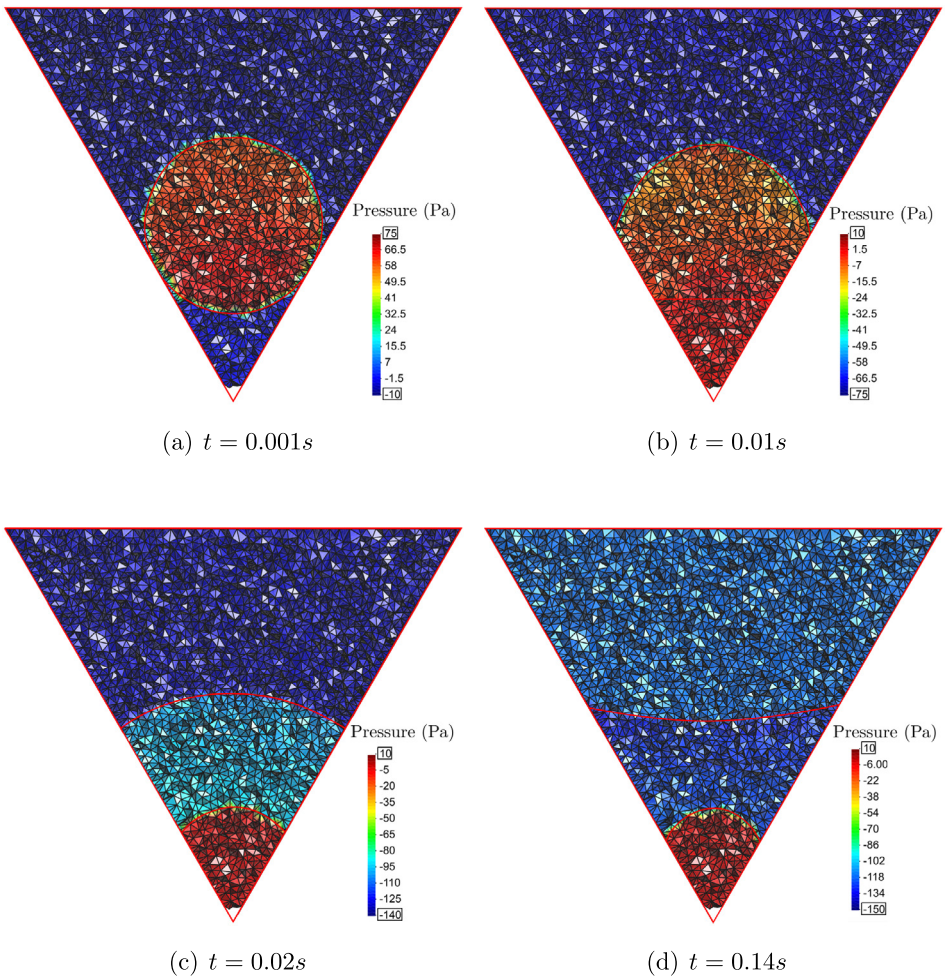

Fig. 23. Pressure contours for $\alpha = 60°$. At $t = 0.14s$, the system has almost reached its equilibrium configuration.

In order to improve the coupling between the momentum equation and the evolving interface that is represented by the level-set function, in this work the level-set convection equation is split in time as shown in Algorithm 1. Numerical simulations showed that such splitting could positively affect the accuracy of the method and alleviate the need for an excessive diffusive level-set smoothing to regularize the interface. Nevertheless, further investigations are needed to quantify this improvement.

CRediT authorship contribution statement

Mohammad R. Hashemi: Conceptualization, Methodology, Software, Writing – original draft. **Pavel B. Ryzhakov:** Conceptualization, Funding acquisition, Methodology, Supervision, Writing – review & editing. **Riccardo Rossi:** Conceptualization, Methodology, Supervision, Writing – review & editing.

Declaration of competing interest

The authors of the present work declare that they have no conflict of interests.

Acknowledgements

This work was performed within the framework of AMADEUS project ("Advanced Multi-scAle moDEling of coupled mass transport for improving water management in fUel cellS", reference number PGC2018-101655-B-I00) supported by the *Ministerio de Ciencia, Innovación y Universidades* of Spain. The authors also acknowledge financial support of the mentioned Ministry via the "Severo Ochoa Programme" for Centres of Excellence in R&D (reference: CEX2018-000797-S) given to the International Centre for Numerical Methods in Engineering (CIMNE).

References

[1] D. Bonn, J. Eggers, J. Indekeu, J. Meunier, E. Rolley, Wetting and spreading, Rev. Mod. Phys. 81 (2009) 739–805, https://doi.org/10.1103/RevModPhys.81.739.

[2] C.N. Baroud, H. Willaime, Multiphase flows in microfluidics, C. R. Phys. 5 (2004) 547–555, https://doi.org/10.1016/j.crhy.2004.04.006, http://www.sciencedirect.com/science/article/pii/S1631070504000854.

[3] L. Shui, J.C.T. Eijkel, A. van den Berg, Multiphase flow in microfluidic systems – control and applications of droplets and interfaces, Adv. Colloid Interface Sci. 133 (2007) 35–49, https://doi.org/10.1016/j.cis.2007.03.001, http://www.sciencedirect.com/science/article/pii/S0001868607000590.

[4] K.A. Culligan, D. Wildenschild, B.S.B. Christensen, W.G. Gray, M.L. Rivers, Pore-scale characteristics of multiphase flow in porous media: a comparison of air–water and oil–water experiments, Adv. Water Resour. 29 (2006) 227–238, https://doi.org/10.1016/j.advwatres.2005.03.021, http://www.sciencedirect.com/science/article/pii/S030917080500120X.

[5] K.E. Thompson, Pore-scale modeling of fluid transport in disordered fibrous materials, AIChE J. 48 (2002) 1369–1389, https://doi.org/10.1002/aic.690480703, http://aiche.onlinelibrary.wiley.com/doi/abs/10.1002/aic.690480703.

[6] X. Zhu, P. Sui, N. Djilali, Three-dimensional numerical simulations of water droplet dynamics in a PEMFC gas channel, J. Power Sources 181 (2008) 101–115, https://doi.org/10.1016/j.jpowsour.2008.03.005, https://linkinghub.elsevier.com/retrieve/pii/S0378775308004989.

[7] M. Andersson, S.B. Beale, M. Espinoza, Z. Wu, W. Lehnert, A review of cell-scale multiphase flow modeling, including water management, in polymer electrolyte fuel cells, Appl. Energy 180 (2016) 757–778, https://doi.org/10.1016/j.apenergy.2016.08.010, http://www.sciencedirect.com/science/article/pii/S0306261916310972.

[8] A.Z. Weber, R.L. Borup, R.M. Darling, P.K. Das, T.J. Dursch, W. Gu, D. Harvey, A. Kusoglu, S. Litster, M.M. Mench, R. Mukundan, J.P. Owejan, J.G. Pharoah, M. Secanell, I.V. Zenyuk, A critical review of modeling transport phenomena in polymer-electrolyte fuel cells, J. Electrochem. Soc. 161 (2014) F1254–F1299, https://doi.org/10.1149/2.0751412jes, https://iopscience.iop.org/article/10.1149/2.0751412jes.

[9] A. Jarauta, P. Ryzhakov, Challenges in computational modeling of two-phase transport in polymer electrolyte fuel cells flow channels: a review, Arch. Comput. Methods Eng. 25 (2018) 1027–1057, https://doi.org/10.1007/s11831-017-9243-2, http://link.springer.com/10.1007/s11831-017-9243-2.

[10] J.H. Snoeijer, B. Andreotti, Moving contact lines: scales, regimes, and dynamical transitions, Annu. Rev. Fluid Mech. 45 (2013) 269–292, https://doi.org/10.1146/annurev-fluid-011212-140734, http://www.annualreviews.org/doi/10.1146/annurev-fluid-011212-140734.

[11] Y.D. Shikhmurzaev, Moving contact lines and dynamic contact angles: a 'litmus test' for mathematical models, accomplishments and new challenges, Eur. Phys. J. Spec. Top. 229 (2020) 1945–1977, https://doi.org/10.1140/epjst/e2020-900236-8.

[12] C. Huh, L.E. Scriven, Hydrodynamic model of steady movement of a solid/liquid/fluid contact line, J. Colloid Interface Sci. 35 (1971) 85–101.

[13] E.B. Dussan, S.H. Davis, On the motion of a fluid-fluid interface along a solid surface, J. Fluid Mech. 65 (1974) 71–95, https://doi.org/10.1017/S0022112074001261, https://www.cambridge.org/core/product/identifier/S0022112074001261/type/journal_article.

[14] L.M. Hocking, A moving fluid interface, Part 2: the removal of the force singularity by a slip flow, J. Fluid Mech. 79 (1977) 209–229, https://doi.org/10.1017/S0022112077000123, https://www.cambridge.org/core/product/identifier/S0022112077000123/type/journal_article.

[15] L.M. Hocking, A.D. Rivers, The spreading of a drop by capillary action, J. Fluid Mech. 121 (1982) 425, https://doi.org/10.1017/S0022112082001979, http://www.journals.cambridge.org/abstract_S0022112082001979.

[16] P.A. Thompson, M.O. Robbins, Simulations of contact-line motion: slip and the dynamic contact angle, Phys. Rev. Lett. 63 (1989) 766.

[17] T. Qian, X.-P. Wang, P. Sheng, Power-law slip profile of the moving contact line in two-phase immiscible flows, Phys. Rev. Lett. 93 (2004) 094501, https://doi.org/10.1103/PhysRevLett.93.094501, https://link.aps.org/doi/10.1103/PhysRevLett.93.094501.

[18] T. Qian, X.-P. Wang, P. Sheng, Molecular hydrodynamics of the moving contact line in two-phase immiscible flows, preprint, arXiv:cond-mat/0510403, 2005.

[19] R.G. Cox, The dynamics of the spreading of liquids on a solid surface. Part 1. Viscous flow, J. Fluid Mech. 168 (1986) 169, https://doi.org/10.1017/S0022112086000332, http://www.journals.cambridge.org/abstract_S0022112086000332.

[20] P. Zhang, K. Mohseni, Theoretical model of a finite force at the moving contact line, Int. J. Multiph. Flow 132 (2020) 103398, https://doi.org/10.1016/j.ijmultiphaseflow.2020.103398, http://www.sciencedirect.com/science/article/pii/S0301932220305073.

[21] T.D. Blake, J.M. Haynes, Kinetics of liquid/liquid displacement, J. Colloid Interface Sci. 30 (1969) 421–423, https://doi.org/10.1016/0021-9797(69)90411-1, http://www.sciencedirect.com/science/article/pii/0021979769904111.

[22] T.D. Blake, A. Clarke, J. De Coninck, M.J. de Ruijter, Contact angle relaxation during droplet spreading: comparison between molecular kinetic theory and molecular dynamics, Langmuir 13 (1997) 2164–2166, https://doi.org/10.1021/la962004g.

[23] M.J. de Ruijter, T.D. Blake, J. De Coninck, Dynamic wetting studied by molecular modeling simulations of droplet spreading, Langmuir 15 (1999) 7836–7847, https://doi.org/10.1021/la990171l.

[24] J.G. Petrov, J. Ralston, M. Schneemilch, R.A. Hayes, Dynamics of partial wetting and dewetting in well-defined systems, J. Phys. Chem. B 107 (2003) 1634–1645, https://doi.org/10.1021/jp026723h.

[25] T.D. Blake, The physics of moving wetting lines, J. Colloid Interface Sci. 299 (2006) 1–13, https://doi.org/10.1016/j.jcis.2006.03.051, https://linkinghub.elsevier.com/retrieve/pii/S0021979706002463.

[26] D. Seveno, A. Vaillant, R. Rioboo, H. Adao, J. Conti, J. De Coninck, Dynamics of wetting revisited, Langmuir 25 (2009) 13034–13044.

[27] M.J. de Ruijter, J. De Coninck, T.D. Blake, A. Clarke, A. Rankin, Contact angle relaxation during the spreading of partially wetting drops, Langmuir 13 (1997) 7293–7298, https://doi.org/10.1021/la970825v.

[28] S.R. Ranabothu, C. Karnezis, L.L. Dai, Dynamic wetting: hydrodynamic or molecular-kinetic?, J. Colloid Interface Sci. 288 (2005) 213–221, https://doi.org/10.1016/j.jcis.2005.02.074, http://www.sciencedirect.com/science/article/pii/S0021979705002316.

[29] A. Mohammad Karim, S.H. Davis, H.P. Kavehpour, Forced versus spontaneous spreading of liquids, Langmuir 32 (2016) 10153–10158, https://doi.org/10.1021/acs.langmuir.6b00747.

[30] W. Ren, D. Hu, W. E, Continuum models for the contact line problem, Phys. Fluids 22 (2010) 102103, https://doi.org/10.1063/1.3501317, https://aip-scitation-org.recursos.biblioteca.upc.edu/doi/full/10.1063/1.3501317.

[31] P. Petrov, I. Petrov, A combined molecular-hydrodynamic approach to wetting kinetics, Langmuir 8 (1992) 1762–1767.

[32] F. Brochard-Wyart, P.G. de Gennes, Dynamics of partial wetting, Adv. Colloid Interface Sci. 39 (1992) 1–11, https://doi.org/10.1016/0001-8686(92)80052-Y, http://www.sciencedirect.com/science/article/pii/000186869280052Y.

[33] M.J. de Ruijter, J. De Coninck, G. Oshanin, Droplet spreading: partial wetting regime revisited, Langmuir 15 (1999) 2209–2216, https://doi.org/10.1021/la971301y.

[34] M.J. de Ruijter, M. Charlot, M. Voué, J. De Coninck, Experimental evidence of several time scales in drop spreading, Langmuir 16 (2000) 2363–2368, https://doi.org/10.1021/la990769t.

[35] C.M. Phan, A.V. Nguyen, G.M. Evans, Combining hydrodynamics and molecular kinetics to predict dewetting between a small bubble and a solid surface, J. Colloid Interface Sci. 296 (2006) 669–676, https://doi.org/10.1016/j.jcis.2005.09.062, http://www.sciencedirect.com/science/article/pii/S0021979705010076.

[36] J.-C. Fernández-Toledano, T.D. Blake, J. De Coninck, Taking a closer look: a molecular-dynamics investigation of microscopic and apparent dynamic contact angles, J. Colloid Interface Sci. 587 (2021) 311–323, https://doi.org/10.1016/j.jcis.2020.12.013, https://www.sciencedirect.com/science/article/pii/S0021979720316672.

[37] T. Qian, X.-P. Wang, P. Sheng, Molecular scale contact line hydrodynamics of immiscible flows, Phys. Rev. E 68 (2003) 016306.
[38] T. Qian, X.-P. Wang, P. Sheng, A variational approach to moving contact line hydrodynamics, J. Fluid Mech. 564 (2006) 333, https://doi.org/10.1017/S0022112006001935, http://www.journals.cambridge.org/abstract_S0022112006001935.
[39] W. Ren, W. E, Boundary conditions for the moving contact line problem, Phys. Fluids 19 (2007) 022101.
[40] X. Xu, Y. Di, H. Yu, Sharp-interface limits of a phase-field model with a generalized Navier slip boundary condition for moving contact lines, J. Fluid Mech. 849 (2018) 805–833, https://doi.org/10.1017/jfm.2018.428, https://www.cambridge.org/core/product/identifier/S0022112018004287/type/journal_article.
[41] W. Ren, E. Weinan, Derivation of continuum models for the moving contact line problem based on thermodynamic principles, Commun. Math. Sci. 9 (2011) 597–606, https://doi.org/10.4310/CMS.2011.v9.n2.a13, http://www.intlpress.com/site/pub/pages/journals/items/cms/content/vols/0009/0002/a013/.
[42] S. Manservisi, R. Scardovelli, A variational approach to the contact angle dynamics of spreading droplets, Comput. Fluids 38 (2009) 406–424.
[43] S. Guo, M. Gao, X. Xiong, Y.J. Wang, X. Wang, P. Sheng, P. Tong, Direct measurement of friction of a fluctuating contact line, Phys. Rev. Lett. 111 (2013) 026101, https://doi.org/10.1103/PhysRevLett.111.026101.
[44] Y. Yamamoto, T. Ito, T. Wakimoto, K. Katoh, Numerical simulations of spontaneous capillary rise with very low capillary numbers using a front-tracking method combined with generalized Navier boundary condition, Int. J. Multiph. Flow 51 (2013) 22–32.
[45] J. Zhang, P. Yue, A level-set method for moving contact lines with contact angle hysteresis, J. Comput. Phys. (2020) 109636.
[46] E. Mahrous, A. Jarauta, T. Chan, P. Ryzhakov, A.Z. Weber, R.V. Roy, M. Secanell, A particle finite element-based model for droplet spreading analysis, Phys. Fluids 32 (2020) 042106.
[47] S. Zahedi, K. Gustavsson, G. Kreiss, A conservative level set method for contact line dynamics, J. Comput. Phys. 228 (2009) 6361–6375.
[48] D. Jacqmin, Contact-line dynamics of a diffuse fluid interface, J. Fluid Mech. 402 (2000) 57–88, https://doi.org/10.1017/S0022112099006874, https://www.cambridge.org/core/product/identifier/S0022112099006874/type/journal_article.
[49] P. Yue, J.J. Feng, Wall energy relaxation in the Cahn–Hilliard model for moving contact lines, Phys. Fluids 23 (2011) 012106, https://doi.org/10.1063/1.3541806, https://aip-scitation-org.recursos.biblioteca.upc.edu/doi/full/10.1063/1.3541806.
[50] Y. Sui, H. Ding, P.D. Spelt, Numerical simulations of flows with moving contact lines, Annu. Rev. Fluid Mech. 46 (2014) 97–119, https://doi.org/10.1146/annurev-fluid-010313-141338.
[51] O. Weinstein, L. Pismen, Scale dependence of contact line computations, Math. Model. Nat. Phenom. 3 (2008) 98–107.
[52] F. Schönfeld, S. Hardt, Dynamic contact angles in CFD simulations, Comput. Fluids 38 (2009) 757–764, https://doi.org/10.1016/j.compfluid.2008.05.007, http://www.sciencedirect.com/science/article/pii/S0045793008001916.
[53] J.-B. Dupont, D. Legendre, Numerical simulation of static and sliding drop with contact angle hysteresis, J. Comput. Phys. 229 (2010) 2453–2478.
[54] Y. Sui, P.D. Spelt, An efficient computational model for macroscale simulations of moving contact lines, J. Comput. Phys. 242 (2013) 37–52.
[55] S. Afkhami, S. Zaleski, M. Bussmann, A mesh-dependent model for applying dynamic contact angles to VOF simulations, J. Comput. Phys. 228 (2009) 5370–5389.
[56] Y. Yamamoto, K. Tokieda, T. Wakimoto, T. Ito, K. Katoh, Modeling of the dynamic wetting behavior in a capillary tube considering the macroscopic–microscopic contact angle relation and generalized Navier boundary condition, Int. J. Multiph. Flow 59 (2014) 106–112.
[57] J. Luo, X.Y. Hu, N.A. Adams, Curvature boundary condition for a moving contact line, J. Comput. Phys. 310 (2016) 329–341, https://doi.org/10.1016/j.jcp.2016.01.024, http://www.sciencedirect.com/science/article/pii/S0021999116000322.
[58] S.O. Unverdi, G. Tryggvason, A front-tracking method for viscous, incompressible, multi-fluid flows, J. Comput. Phys. 100 (1992) 25–37.
[59] Y.-C. Chang, T. Hou, B. Merriman, S. Osher, A level set formulation of Eulerian interface capturing methods for incompressible fluid flows, J. Comput. Phys. 124 (1996) 449–464.
[60] M. Sussman, S. Uto, A computational study of the spreading of oil underneath a sheet of ice, CAM Rep. 114 (1998) 146–159.
[61] J.U. Brackbill, D.B. Kothe, C. Zemach, A continuum method for modeling surface tension, J. Comput. Phys. 100 (1992) 335–354.
[62] J.-J. Xu, W. Ren, A level-set method for two-phase flows with moving contact line and insoluble surfactant, J. Comput. Phys. 263 (2014) 71–90, https://doi.org/10.1016/j.jcp.2014.01.012, https://linkinghub.elsevier.com/retrieve/pii/S0021999114000394.
[63] A. Jarauta, P. Ryzhakov, M. Secanell, P.R. Waghmare, J. Pons-Prats, Numerical study of droplet dynamics in a polymer electrolyte fuel cell gas channel using an embedded Eulerian-Lagrangian approach, J. Power Sources 323 (2016) 201–212, https://doi.org/10.1016/j.jpowsour.2016.05.030, https://linkinghub.elsevier.com/retrieve/pii/S0378775316305687.
[64] P.B. Ryzhakov, A. Jarauta, M. Secanell, J. Pons-Prats, On the application of the PFEM to droplet dynamics modeling in fuel cells, Comput. Part. Mech. 4 (2017) 285–295, https://doi.org/10.1007/s40571-016-0112-9.
[65] M.R. Hashemi, P.B. Ryzhakov, R. Rossi, An enriched finite element/level-set method for simulating two-phase incompressible fluid flows with surface tension, Comput. Methods Appl. Mech. Eng. 370 (2020) 113277, https://doi.org/10.1016/j.cma.2020.113277, http://www.sciencedirect.com/science/article/pii/S004578252030462X.
[66] G.C. Buscaglia, R.F. Ausas, Variational formulations for surface tension, capillarity and wetting, Comput. Methods Appl. Mech. Eng. 200 (2011) 3011–3025.
[67] R.G. Cox, Inertial and viscous effects on dynamic contact angles, J. Fluid Mech. 357 (1998) 249–278, https://doi.org/10.1017/S0022112097008112, http://www.cambridge.org/core/journals/journal-of-fluid-mechanics/article/inertial-and-viscous-effects-on-dynamic-contact-angles/02C101E9C7C2119FCC2EEE58BDF14C1F.
[68] M. Wörner, X. Cai, H. Alla, P. Yue, A semi-analytical method to estimate the effective slip length of spreading spherical-cap shaped droplets using Cox theory, Fluid Dyn. Res. 50 (2018) 035501, https://doi.org/10.1088/1873-7005/aaaef6.
[69] Y.D. Shikhmurzaev, Spreading of drops on solid surfaces in a quasi-static regime, Phys. Fluids 9 (1997) 266–275, https://doi.org/10.1063/1.869147, https://aip.scitation.org/doi/abs/10.1063/1.869147.
[70] E.B. Dussan, On the spreading of liquids on solid surfaces: static and dynamic contact lines, Annu. Rev. Fluid Mech. 11 (1979) 371–400, https://doi.org/10.1146/annurev.fl.11.010179.002103, http://www.annualreviews.org/doi/10.1146/annurev.fl.11.010179.002103.
[71] T. Young III, An essay on the cohesion of fluids, Philos. Trans. R. Soc. Lond. 95 (1805) 65–87, https://doi.org/10.1098/rstl.1805.0005, https://royalsocietypublishing-org.recursos.biblioteca.upc.edu/doi/abs/10.1098/rstl.1805.0005.
[72] D. Seveno, T.D. Blake, J. De Coninck, Young's equation at the nanoscale, Phys. Rev. Lett. 111 (2013) 096101, https://doi.org/10.1103/PhysRevLett.111.096101.
[73] L.M. Pismen, Some singular errors near the contact line singularity, and ways to resolve both, Eur. Phys. J. Spec. Top. 197 (2011) 33, https://doi.org/10.1140/epjst/e2011-01433-0.
[74] D.N. Sibley, N. Savva, S. Kalliadasis, Slip or not slip? A methodical examination of the interface formation model using two-dimensional droplet spreading on a horizontal planar substrate as a prototype system, Phys. Fluids 24 (2012) 082105, https://doi.org/10.1063/1.4742895, https://aip.scitation.org/doi/abs/10.1063/1.4742895.
[75] R. Zorrilla, A. Larese, R. Rossi, A modified Finite Element formulation for the imposition of the slip boundary condition over embedded volumeless geometries, Comput. Methods Appl. Mech. Eng. 353 (2019) 123–157.
[76] Y. Wei, E. Rame, L.M. Walker, S. Garoff, Dynamic wetting with viscous Newtonian and non-Newtonian fluids, J. Phys., Condens. Matter 21 (2009) 464126, https://doi.org/10.1088/0953-8984/21/46/464126.

[77] L. Chen, J. Yu, H. Wang, Convex nanobending at a moving contact line: the missing mesoscopic link in dynamic wetting, ACS Nano 8 (2014) 11493–11498, https://doi.org/10.1021/nn5046486.
[78] R. Codina, S. Badia, J. Baiges, J. Principe, Variational multiscale methods in computational fluid dynamics, Second Edition, in: Encyclopedia of Computational Mechanics, Wiley Online Library, 2018, pp. 1–28.
[79] M. Sussman, P. Smereka, S. Osher, A level set approach for computing solutions to incompressible two-phase flow, J. Comput. Phys. 114 (1994) 146–159.
[80] R. Codina, A discontinuity-capturing crosswind-dissipation for the finite element solution of the convection-diffusion equation, Comput. Methods Appl. Mech. Eng. 110 (1993) 325–342, https://doi.org/10.1016/0045-7825(93)90213-H, http://www.sciencedirect.com/science/article/pii/004578259390213H.
[81] M.F. Trujillo, L. Anumolu, D. Ryddner, The distortion of the level set gradient under advection, J. Comput. Phys. 334 (2017) 81–101.
[82] S. Groß, V. Reichelt, A. Reusken, A finite element based level set method for two-phase incompressible flows, Comput. Vis. Sci. 9 (2006) 239–257.
[83] C. Min, On reinitializing level set functions, J. Comput. Phys. 229 (2010) 2764–2772.
[84] G. Della Rocca, G. Blanquart, Level set reinitialization at a contact line, J. Comput. Phys. 265 (2014) 34–49.
[85] R.N. Elias, M.A. Martins, A.L. Coutinho, Simple finite element-based computation of distance functions in unstructured grids, Int. J. Numer. Methods Eng. 72 (2007) 1095–1110.
[86] A.-K. Tornberg, B. Engquist, A finite element based level-set method for multiphase flow applications, Comput. Vis. Sci. 3 (2000) 93–101.
[87] P. Dadvand, R. Rossi, E. Oñate, An object-oriented environment for developing finite element codes for multi-disciplinary applications, Arch. Comput. Methods Eng. 17 (2010) 253–297, https://doi.org/10.1007/s11831-010-9045-2, http://link.springer.com/10.1007/s11831-010-9045-2.
[88] D. Demidov, AMGCL: an efficient, flexible, and extensible algebraic multigrid implementation, Lobachevskii J. Math. 40 (2019) 535–546.
[89] H. Lamb, Hydrodynamics, University Press, 1924.